

Article

Structural and Spectroscopic Characteristics of Ni^{II} and Cu^{II} Complexes with Poly (Vinyl Alcohol-Nicotinic Acid) Copolymers for Photocatalytic Degradation of Indigo Carmine Dye

Ibraheem O. Ali ¹, Hisham S. Nassar ^{2,3}, Ahmed M. Naglah ^{4,5} , Laila M. Al-Harbi ⁶ 
and Ahmed A. Elhenawy ^{2,3,*}

¹ Chemistry Department, College of Science and Arts, Jouf University, Al-Qurayyat 77455, Saudi Arabia; iothmana@ju.edu.sa

² Department of Chemistry, Faculty of Science, Al-Azhar University, Nasr City, Cairo 11884, Egypt; h_nassar5@yahoo.com

³ Chemistry Department, Faculty of Sciences and Arts, Albaha University, Al-Mikwah Branch, Al-Mikwah 65311, Saudi Arabia

⁴ Department of Pharmaceutical Chemistry, Drug Exploration & Development Chair (DEDC), College of Pharmacy, King Saud University, Riyadh 11451, Saudi Arabia; anaglah@ksu.edu.sa

⁵ National Research Centre, Peptide Chemistry Department, Chemical Industries Research Division, Dokki, Cairo 12622, Egypt

⁶ Chemistry Department, King Abdulaziz University, Jeddah 80203, Saudi Arabia; Lalharbi1@ksu.edu.sa

* Correspondence: ahmed.elhenawy@azhar.edu.eg; Tel.: +9-665-9904-4526



Citation: Ali, I.O.; Nassar, H.S.; Naglah, A.M.; Al-Harbi, L.M.; Elhenawy, A.A. Structural and Spectroscopic Characteristics of Ni^{II} and Cu^{II} Complexes with Poly (Vinyl Alcohol-Nicotinic Acid) Copolymers for Photocatalytic Degradation of Indigo Carmine Dye. *Crystals* **2021**, *11*, 1244. <https://doi.org/10.3390/cryst11101244>

Academic Editor: Roberto Comparelli

Received: 11 May 2021

Accepted: 8 October 2021

Published: 14 October 2021

Publisher's Note: MDPI stays neutral with regard to jurisdictional claims in published maps and institutional affiliations.



Copyright: © 2021 by the authors. Licensee MDPI, Basel, Switzerland. This article is an open access article distributed under the terms and conditions of the Creative Commons Attribution (CC BY) license (<https://creativecommons.org/licenses/by/4.0/>).

Abstract: Poly-vinyl-alcohol (PVA) has been cross-linked chemically with nicotinic-acid (NA) in an aqueous medium. The copolymers were complexed with Ni^{II} and Cu^{II} ions. The complexes and copolymers were analyzed using FT-IR and UV-Visible spectroscopy, XRD and TGA, but copolymers were extra analyzed with nuclear magnetic resonance (¹H NMR). FT-IR spectra of copolymer revealed the presence of C=O & C-N groups due to the esterification of PVA-NA. The Cu/NA-PVA formed via bidentate interaction of the pyridinyl and carboxyl of NA. EPR/UV-vis data shows the square-planar geometry for Ni^{II} and Cu^{II} complexes. The adsorption of IC dye onto Cu^{II}/NA-PVA complex was noticeably greater (90%) in 35 min than Ni^{II}/NA-PVA. The DFT\B3LYP with 6-311G* quantum chemical calculations were carried out for tested compounds. The DFT was conducted to examine an interaction mode of the target compounds with the reaction system. The QSPR was calculated as: optimization geometries, (FMOs), chemical-reactivities and NLO for the copolymers. The (MEPs) were figured to predict the interaction behavior of the ligand and its complexes.

Keywords: copolymers; metal complexes; Indigo-carmine-dye; DFT

1. Introduction

Artificial dyes are most commonly used in fabric and skin treatment manufacturing [1]. Dyes cause harmful effects in the environment, even in low concentrations. In addition, there are other highly toxic compounds in the discharge of colored wastewater that increase environmental problems [2,3]. These wastes, released from fabric and skin treatment manufacturing, having 1 mg/L of dye, are sufficient to impart color to H₂O, thus making it unpotable for everyday use [4,5]. Treatments used for color removal (chemical, physical, biological or hybrid) have been highly effective in removing color [3,6]. However, chemical, and physical treatments have the disadvantage of generating sludge that is difficult to handle, expensive, and requires large treatment areas [3,7]

Coordination polymers (CPs) can be useful in several fields, for example, gas adsorption and packing, drug supply, various catalysis, electronic devices, magnetism, photoluminescence, and others [8–11]. To the best of our knowledge, the mixed-ligands strategy,

incorporating the multicarboxylate and N-donor ligands, is beneficial to form new CPs and further construct multifunctional materials. Moreover, as a consequence of the interpenetration, CPs may be used as potential super-hard, porous, and magnetic materials [12].

Additionally, the barrier properties and thermal stability of PVA have increased by changed cross-links with boric acid mixture films [13,14]. Carlotti et al. obtained water soluble PVA-Lactic acid with no catalysts [15]. The mixture of PVA, chitosan and AgNO_3 has been previously used for electrospun nanofibers with antibacterial activity [16].

Pyridyl carboxylic acids and their N-oxide products are particularly suitable in this regard. On the other hand, the mistreatment of the ligand with open-framework products remains insufficient [17,18]. Nevertheless, the actions of ligand vis CPs are still incomplete; the metal ion (MI) in CPs of N-oxides based on NA have been structurally studied [19]. Complexation of NA against several metals (Mn, Co, Ni, Cu & Zn) were reported [20].

Many researchers have carried out studies on CPs of transition metals with suitable ligands [1]. Various Cu(II) containing CPs with diverse geometries play an important role in catalytic applications [2]. Cu NPs based catalysts or Cu complexes immobilized on polymers can be obtained by different processes such as metallic or ionic Cu. In 2008, Orto et al. reported the fabrication and application of Cu(II)- polyampholyte as an effective catalyst for methyl orange (MO) degradation as a pollutant at room temperature via H_2O_2 activation [3].

In this paper, we report synthesis and characterization of PVA copolymers using Nicotinic acid as monomer. Coordination polymers of NA-PVA with Metal ions (CuII and NiII) were prepared by incipient wetness impregnation method. CPs offer a good photocatalytic performance, non-toxicity, and low production costs. A new complex CuII-/or NiII/NA-PVA: we expected, the novelty CuII and NiII complex to provide a promising way for photocatalytic degradation of Indigo carmine dye (IC) as applications in wastewater treatment. Physico-chemical features for the investigated Cps and its complexes were analyzed using different spectral data (FT-IR, UV/Vis, NMR, ESR, TGA and X-ray- analysis).

2. Materials and Methods

2.1. Materials & Instruments

The chemicals used are listed in Supplementary Materials.

2.1.1. Synthesis of Copolymer

PVA-CPs based in NA as monomer were prepared, as previously described elsewhere [12]. PVA-NA was prepared via the substance reaction of PVA and NA in equal molar ratio. PVA (0.3 g, 6.80 mmol of OH) and NA (0.6 g, 4.76 mmol of COOH) were presented in a 50 mL glass container fixed with an automatic stirrer, a nitrogen inlet, a condensation side-arm joined to a condenser and other arm for receiving flask. Temperature was increased from 383 to 453 K. The end of the reaction was characterized by the full recuperation of the theoretically required amount of water generated by the esterification reaction.

2.1.2. Synthesis of M/PVA-NA Complexes

The incipient wetness impregnation method was used for preparation of M/PVA-NA ($M = \text{Ni}^{\text{II}}, \text{Cu}^{\text{II}}$). The desired metal ions and CP(PVA-NA) were utilized to obtain the acquired distribution of MI (1:1 molar-ratio). Alternatively, metal ions were dissolved in distilled water; then PVA-NA was added, whilst stirring for additional 7 h at 80 °C. The obtained final mixtures were filtered, then washed-away using a distilled H_2O and dried for 12 h at 62.5 °C.

2.2. Catalytic Activity

2.2.1. Decolorization in Air (Adsorption)

Testing decolorization of IC dye on M/PVA-NA in the absence of ultraviolet irradiation were carried out in a batch method, as reported in Supplementary Material.

2.2.2. Photocatalytic Evaluation

All the tests were carried out by a horizontal cylinder annular batch apparatus. IC was designated and preformed as a classical mode [19].

The removal-efficiency% (IC) was calculated by equation:

$$\% \text{Removal} - \text{efficiency} = \frac{C_0 - C}{C_0} \times 100 \quad (1)$$

where C_0 is IC-content and C is IC-retained in solution.

2.3. Molecular Modeling Study & Computational Model

The quantum chemical computations were performed, using MOPAC16 package, then the Gaussian 09W program package, as mentioned in Supplementary Materials.

3. Results & Discussion

3.1. NMR

^1H NMR spectrum (Figure 1) of combination NA-PVA in dimethyl sulfoxide- d_6 expose the supporting signals at $\delta = 7.4\text{--}9.3$ ppm (Ar-H), 3.77 ppm (PVA-CH-OCO-Nicotinic), 3.45 ppm (PVA-OH) and 3.40 ppm (PVA-CH $_2^-$). The resonance of H-OCO-Nicotinic close to 11 ppm disappeared, showing their acid function conversion to ester function is complete.

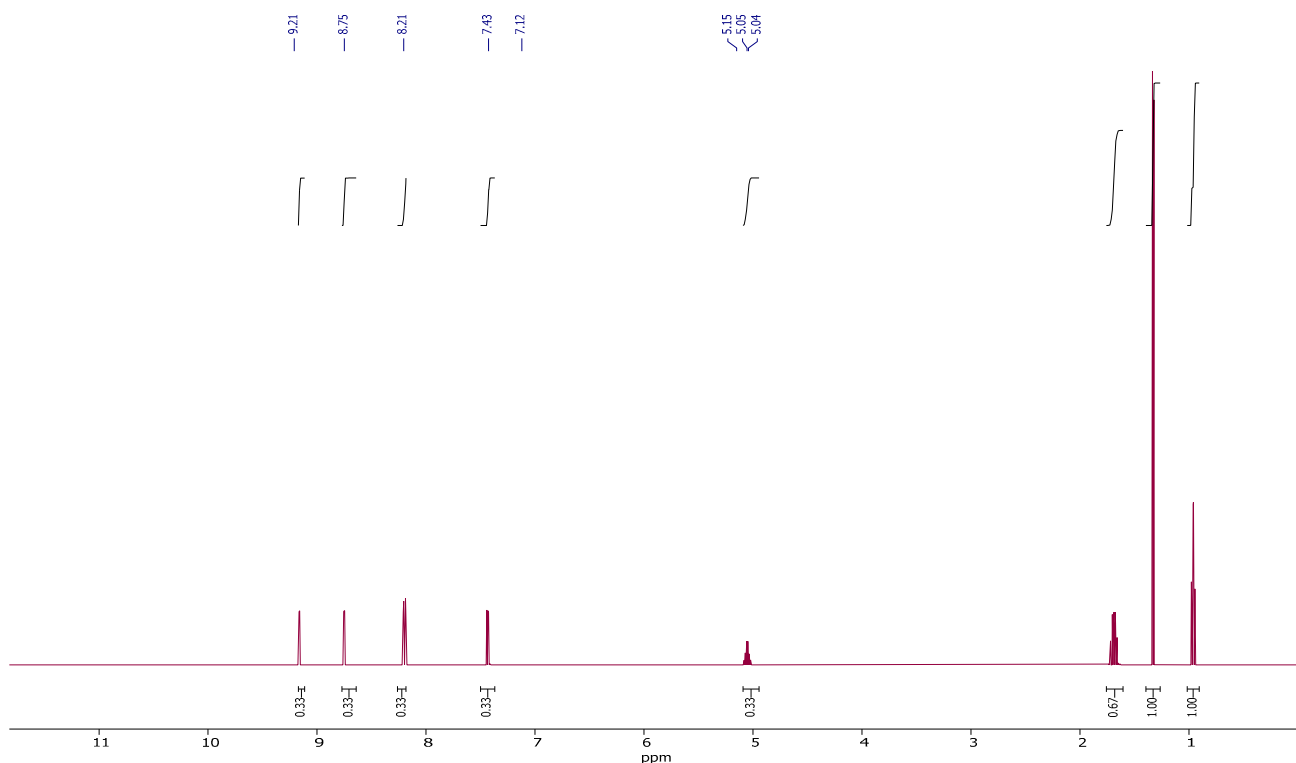


Figure 1. ^1H NMR spectrum of NA-PVA copolymer sample.

3.2. IR Spectra

FT-IR spectra of PVA, NA and PVA-NA are illustrated in Figure 2A. The 3424 & 3411 cm^{-1} bands owing to stretching OH vibration related uncombined PVA and NA, respectively. Bands located at 1646 & 1417 cm^{-1} attributed to the bending mode for OH due to presence of H_2O molecules in parent PVA and NA, respectively. The 2924 , 2852 , 1454 cm^{-1} bands for the parent PVA are due to different modes of CH_2 vibrations (symmetric, anti-symmetric & bending), in PVA carbon chain [21]. The 3071 & 3163 cm^{-1} bands, the one explained by

C–H stretching of NA aromatic ring. The stretching mode for C–O of free PVA appeared at 1037 cm^{-1} [22]. The C–O group in original NA appeared at 1298 cm^{-1} in stretching vibration mode, while the 1709 & 1322 cm^{-1} bands are related to stretching C=O and $\nu(\text{C–N})$, respectively.

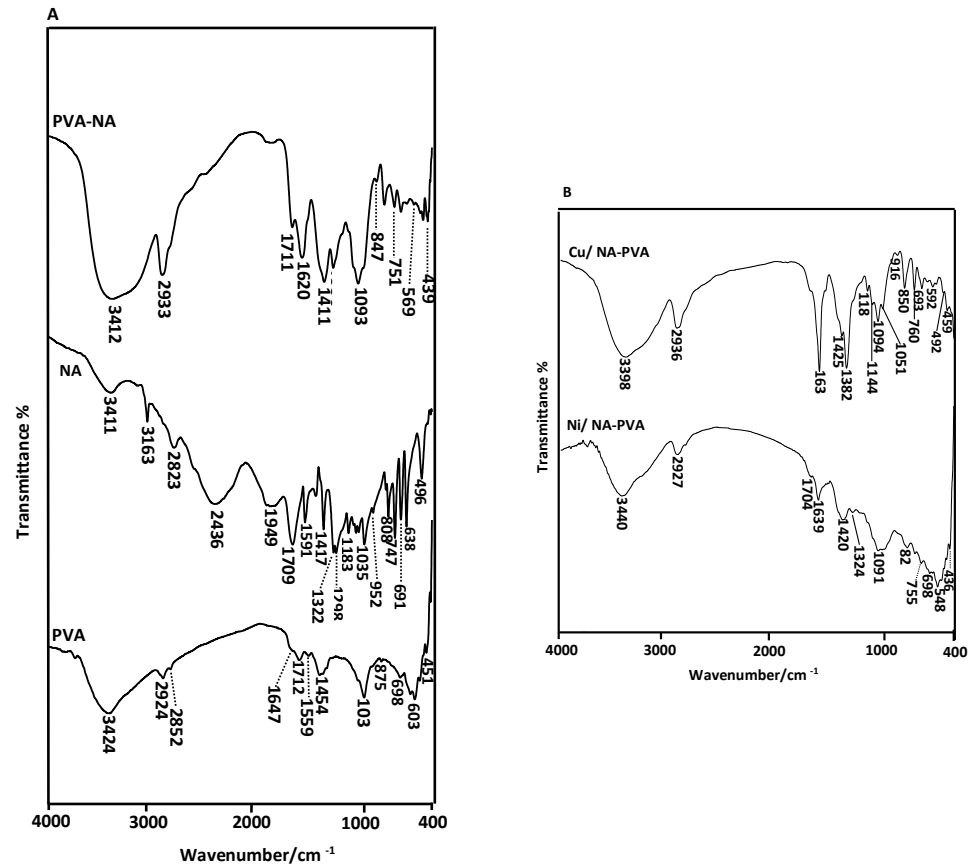


Figure 2. (A) FTIR translation spectra of PVA, NA and PVA-NA samples. (B) FT-IR translation spectra of Ni/PVA-NA and Cu/PVA-NA samples.

IR spectrum of NA-PVA formulations exhibited changing in bands compared to the parent (PVA and NA). Hydroxy group showed in stretching mode and appeared at 3412 cm^{-1} . The absorbed bands at 1711 & 1326 cm^{-1} are related to C=O & $\nu(\text{C–N})$, respectively. These bands are absent in original PVA, which postulated the esterification process occurred between PVA & NA. The C=O group of the ester appeared at 1711 cm^{-1} , while the 1298 cm^{-1} band for C–O of PVA was absent. These results supported NA-PVA nanofibers were cross-linked with the ester bond through thermal treatment.

IR spectra of Ni^{II} and Cu^{II} /PVA-NA formulation was interpreted in Figure 2B. It is well-known that the Cu^{II} /PVA-NA were formed through bi-dentate contact for the nitrogen atom of NA subsequent in a $\nu(\text{C–N})$ shift from 1326 cm^{-1} to a greater range of frequency at 1384 cm^{-1} . The spectrum of Cu-complex was shifted due to bidentate interaction of the pyridinyl ring of NA with COOH group. The low intensity band at 459 cm^{-1} is ascribed to Cu–O vibration [23].

3.3. UV-Visible and EPR Spectra

Figure 3 showed the UV-visible spectra of Ni^{II} and Cu^{II} complexed with NA-PVA. Band at 286 nm assigned to a $\pi \rightarrow \pi^*$ transition: although band at 342 nm associated $n \rightarrow \pi^*$. This transition is due to C=O group connected with ($=\text{C}=\text{C}=\text{C}$) bonds of ($-\text{CH}=\text{CH}$)-CO. The presence of carbonyl functionalities is due to PVA and NA interaction.

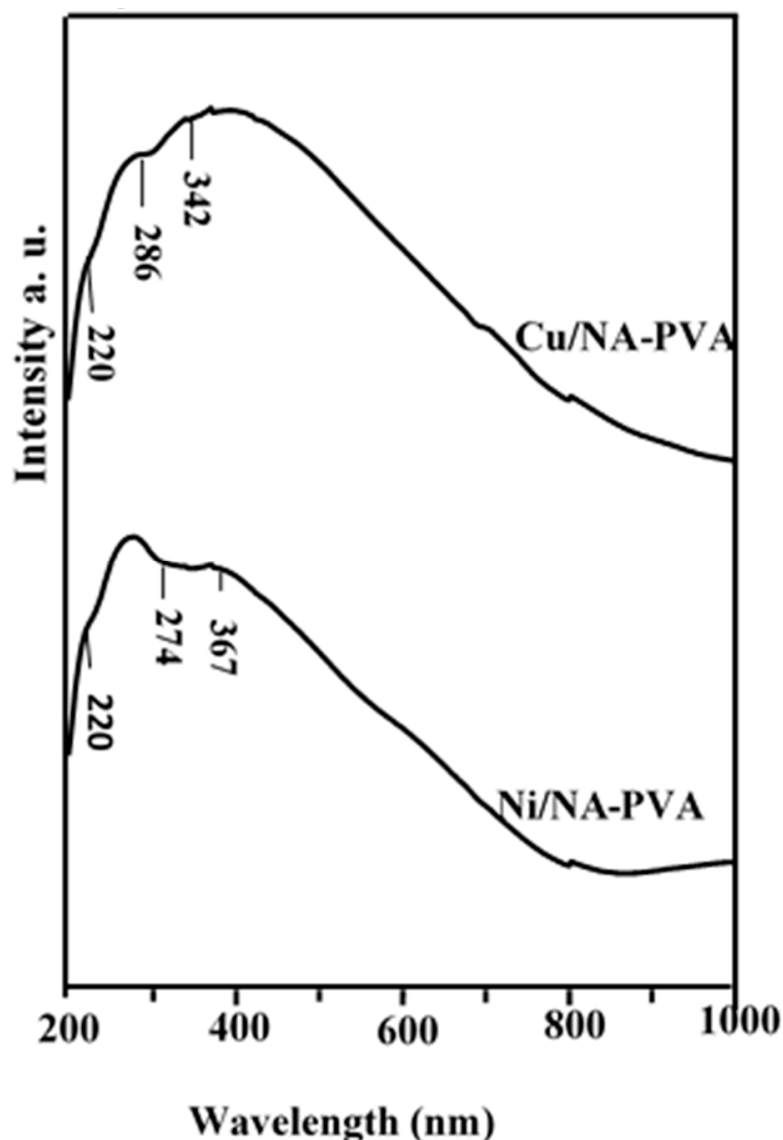


Figure 3. Diffuse reflectance versus wavelength for Ni/PVA-NA and Cu/PVA-NA samples.

Spectra of Ni/NA-PVA complex demonstrated broad band 367 nm is related to the ${}^3A_{2g}(F) \rightarrow {}^3T_{2g}$ with charge transfer transitions, respectively. Thus, the Ni/NA-PVA complex has square planar geometry [24]. On the other hand, Cu^{II}/Cp complex shows a relatively broad band at 342 nm with a low intensity. This band could be ascribed to $({}^2E_g \rightarrow {}^2T_{2g}) M \rightarrow L$ charge transfer transitions, which is consistent with square planar geometry [25].

Figure 4 showed $Ni^{II}/PVA-NA$ & $Cu^{II}/PVA-NA$ EPR spectra. The spectra of EPR for $Cu^{II}/PVA-NA$ showed axial signals with an isotropic component, $g_{||} = 2.163$ and $g_{\perp} = 2.179$. So, the unpaired electron located in the d_{z^2} orbital to obtain ${}^2A_{1g}$ as the ground state with $g_{\perp} > g_{||} > 2$. Thus, $Cu^{II}/PVA-NA$ has square planar geometry around the copper (II) ion [26,27]. No signal appeared at half field in the spectrum, where the possibility of dimeric form of Cu^{II}/CP [28].

The $Ni^{II}/NA-PVA$ shows $g_{||} = 2.009$ and $g_{\perp} = 0$ in Figure 4. From examination of the ESR signals at 3460.410 G, it was deduced that $g_{||} > g_{\perp} > 2.0$ and possess a lengthened octahedral geometry for the CP complexes, the unpaired electron mostly sits in the $d_{x^2-y^2}$ orbital, with maybe some d_{z^2} character due to the slight symmetry, which supports a square planar for $Ni^{II}/NA-PVA$ structure [29,30].

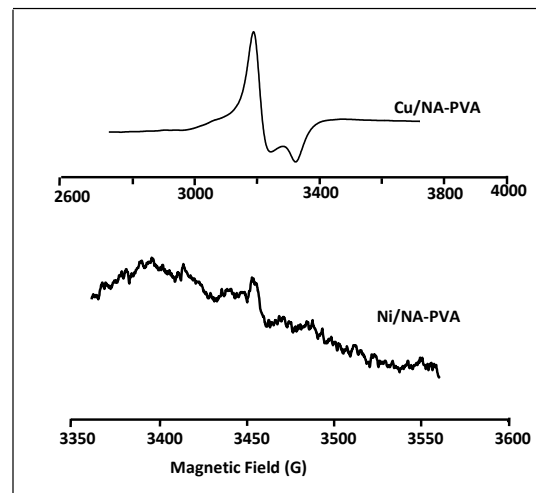


Figure 4. EPR spectra of Ni/PVA-NA and Cu/PVA-NA copolymer samples.

3.4. Thermal Analysis

Thermal-decomposition characters were examined using TG, DTG. PVA-NA, Ni^{II}-, Cu^{II}-/PVA-NA data at a heating rate of 10 °C/min starts 298–973 K and are revealed in Figure 5. TG curve for parent PVA-NA shows weight loss occurs with three-steps of temperatures in the variety 323 to 973 K. First stage: the weight loss of about 32.62% occurred at 323–523 K due to absent of H₂O partials. This related to complete dehydration reaction of PVA-NA in the limited parts of its molecular chain in which the main PVA could be converted into poly-acetylene(–CH=CH–)_n. Second step: the loss of weight with 47.44% corresponds to 523 to 673 K, due to the breakdown of polymeric network. Third step: the range of temperature between 673–973 K with weight loss (15.93%). The NA change of thermal stability in copolymers with PVA higher than parent PVA.

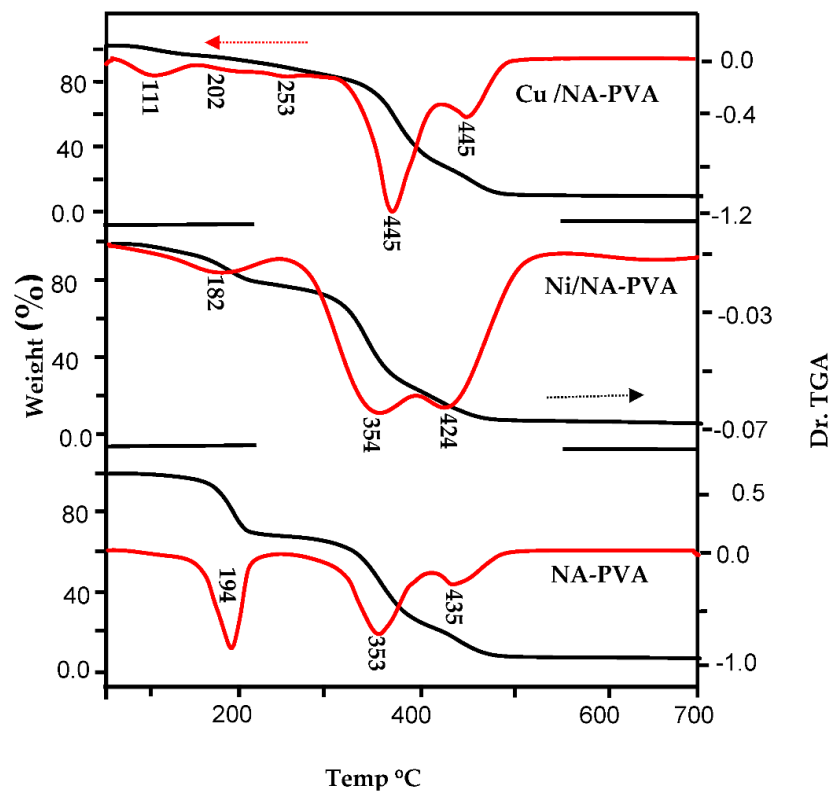


Figure 5. TGA and Dr TGA thermal analysis for Ni/PVA-NA and Cu/PVA-NA copolymer samples.

From analysis of thermal curves of Ni^{II}/PVA-NA & Cu^{II}-/PVA-NA, one can propose three breakdown steps. First step: temperature ranged from 298–498 K exhibited weight-losses 22.44% for Ni^{II}- and 6.31% for Cu^{II}, that conform to loss of hydrated H₂O molecules. Second step starts between 498 and 748 K, corresponding to loss of weight by 53.55%, 10.60% for Ni^{II}&Cu^{II}/PVA-NA, respectively, which related to the breakdown of the polymeric network. The high mass loss in this step is attributable to the release of the PVA-NA molecules. Third step: the mass loss 17.04%, 20.02% for Ni^{II}&Cu^{II}/PVA-NA at temperature range from 498–748 K, with as a result of continuous reduction of the lattice oxygen and preparation of carbon metals/metal oxides.

Thermodynamic activation properties of the structural assets for ligand with metal type through the thermal performance of the complexes, namely, E_a “activation-energy”, ΔH^* “enthalpy”, ΔS^* “entropy”, ΔG^* “Gibbs free energy variation in the breakdown” and the n “order”, were examined beginning with graphically-thermograms for TG and DTG and the equations postulated by Coats–Redfern & Horowitz–Metzger [31,32]. The obtained kinetic parameters are tabled in (Tables 1 and 2). These observations are outlined below:

Table 1. The Kinetic Parameters of NA-PVA, Ni^{II} and Cu/NA-PVA by Coats Redfern program.

Samples	Step	T/K	A/S ⁻¹	E /KJ mol ⁻¹	R ²	ΔH^* /KJmol ⁻¹	ΔS^* /KJ mol ⁻¹ K ⁻¹	ΔG^* /KJmol ⁻¹
NA-PVA	First	466	3.3×10^{15}	170.45	0.97	166.56	0.106	117.06
	Second	626	3.01×10^{-58}	821.12	0.97	815.91	0.43	541.52
	Third	708	1.2×10^{115}	1707.34	0.97	1701.45	-0.13	1794.40
Ni/NA-PVA	First	455	2.5×10^{13}	147.24	0.97	134.45	0.06	113.58
	Second	627	6.3×10^{71}	954.00	0.97	948.78	0.57	586.50
	Third	697	3.6×10^{75}	1121.58	0.96	1115.77	-0.13	1209.67
Cu/NA-PVA	First	384	2.76×10^{13}	124.46	0.996	121.26	0.067	95.252
	Second	475	1.02×10^9	114.92	0.998	110.96	-0.01	119.974
	Third	526	1.94×10^{27}	311.19	0.953	306.80	0.33	132.881
	Four	639	6.24×10^{59}	855.35	0.987	850.03	-0.13	937.052
	Five	718	9.4×10^{118}	1758.72	0.977	1752.74	1.05	996.983

ΔG^* ; activation Gibbs free energy change, ΔH^* ; activation Enthalpy change, ΔS^* ; Entropy change.

Table 2. The Kinetic Parameters of NA-PVA, Ni^{II} and Cu/NA-PVA by Horowitz Metzger program.

Samples	Step	T/K	A/S ⁻¹	E /KJ mol ⁻¹	R2	$\Delta H^*/KJ mol^{-1}$	ΔS^* /KJ mol ⁻¹ K ⁻¹	ΔG^* /KJ mol ⁻¹
NA-PVA	First	466	1.3×1087	800.043	0.96	796.16	1.477	106.335
	Second	626	0.311	0.001	0.97	0.0001	-0.13	0.015
	Third	708	1.3×1052	743.680	0.97	737.79	0.803	169.400
Ni/NA-PVA	First	455	3.5×1004	69.268	0.96	65.480	-0.10	112.882
	Second	627	1.1×1036	450.806	0.97	445.593	0.496	134.225
	Third	697	9.9×1035	519.123	0.96	513.326	0.494	168.396
Cu/NA-PVA	First	384	2.1×1004	56.422	0.99	53.228	-0.10	94.184
	Second	475	2.7×102	54.474	0.998	50.518	-0.14	119.337
	Third	526	2.7×1010	137.781	0.95	133.402	0.007	129.347
	Four	639	1.1×1029	391.437	0.98	386.124	0.362	154.441
	Five	718	1758.729	0.97	0.856	785.812	0.856	170.462

ΔG^* ; activation Gibbs free energy change, ΔH^* ; activation Enthalpy change, ΔS^* ; Entropy change.

ΔS^* has negative value, which revealed that the activated $\text{Ni}^{\text{II}}\&\text{Cu}^{\text{II}}/\text{PVA-NA}$ process take place, and the higher values were ordered with inflexibly of the structure rather than the reactants and intermediate. Thus, the reactions are lower than usual, which is additionally supported by low values [33,34].

Gibbs' free energies were increasing against the following stage for obtained $\text{Ni}^{\text{II}}\&\text{Cu}^{\text{II}}/\text{PVA-NA}$, which reflects that the degree of elimination of the attached ligand will be less than that of the standard ligand [35,36]. This may be due to the inflexibility-structural of the residual $\text{Ni}^{\text{II}}\&\text{Cu}^{\text{II}}/\text{PVA-NA}$ when the explosion of ligands is related to the model complex and needing higher energy, $T\Delta S^*$, for its earlier rearrangement, which is suffering from any structural change.

We noticed a significant gap for E_a values during the first stage at (98–148 kJ mol^{-1}). From Tables 1 and 2, it is apparent that the E_a for $\text{Cu}^{\text{II}}\&\text{Ni}$ -chelates are 124.46 and 147.24 kJ mol^{-1} for the removal of H_2O particles during the hydration process against Cu^{II} - and Ni -chelates, respectively. From these E_a values, we can observe that H_2O with anion particles are simple to remove from the ternary-chelates, in the following order: $\text{Cu}^{\text{II}} > \text{Ni}^{\text{II}}$ -chelates.

Ni^{II} -complex displays a higher thermal stability than $\text{Cu}^{\text{II}}/\text{PVA-NA}$. This can be conferred by electron pairs repulsion in the valence-shell of the central-ion. Cu^{II} has higher electronegativity than Ni^{II} , which is related to a higher repulsive force through bonding-pairs with Cu^{II} valence-shell and decreasing stability [37–39].

The comparable values of ΔG^* for the breakdown stage which relate the similar decomposing particles in the $\text{Ni}^{\text{II}}\&\text{Cu}^{\text{II}}/\text{PVA-NA}$, demonstrating that the mechanism of collapse is the same, and the conclusion of the ligands is more noticeable than that of the divalent metals.

3.5. XRD Studies

Figure 6 exhibited XRD of Ni^{II} - & Cu^{II} -/ PVA-NA copolymers. XRD of the parent PVA-NA copolymers shows a characteristic peak at $2\theta = 19.99^\circ$ and a shoulder at $2\theta = 22.85^\circ$, which can be assigned to the combination of (101) reflection; this is associated with intermolecular-interference between PVA-NA chains (through intermolecular-H-bonding) and (200) crystalline-planes, respectively [40,41]. After complexation with Ni^{II} or Cu with PVA-NA, the peak intensity has been reduced steadily, as can be seen from the XRD-patterns.

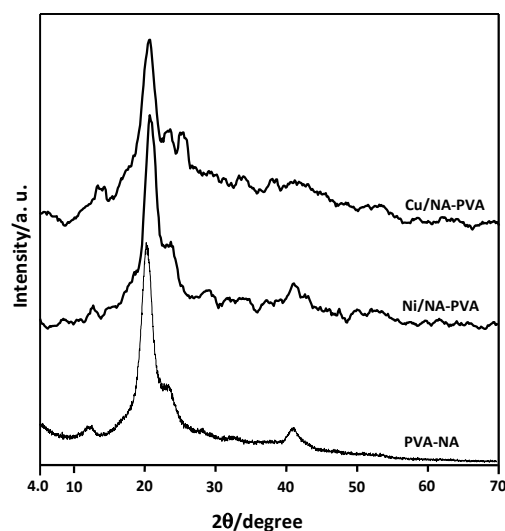


Figure 6. XRD patterns of $\text{Ni}/\text{PVA-NA}$ and $\text{Cu}/\text{PVA-NA}$ samples.

3.6. Band Gap

The optical-energy band-gap (BG) was measured by the Tauc equation [42]. The Kubelka–Munk function is normally useful for changing the diffuse-reflectance into an equivalent-absorption coefficient and generally utilized for evaluating the powder-samples [43]. The Kubelka–Munk-function $F(R)$ was helpful for estimating the energy of Ni^{II} - & Cu^{II} /PVA-NA BG. Thus, a quantity $F(R)$, equal to the coefficient of absorption. The value of α for the Tauc-equation is related with $F(R)$, and interpreted as shown in Equations (3)–(5) in the Supplementary Materials.

The optical BG energy values for Ni^{II} - & Cu^{II} /NA-PVA chelating are (2.0 and 1.19 eV), respectively. The blue-shift in the B.G. of the Cu^{II} /NA-PVA composite may be attributed to supplementary energy levels for sub-BG, induced by the abundant surface and interface defects in the agglomerated particles [44]. The promising property in this case was directed linking of grain-size-nanocrystals with optical BG. The energy of the optical-band was increased slightly and related to the reduced crystallite-size, which promotes a weak quantum-size-effect [45–48]. The difference of the BG with increasing atomic-size is a promising aspect for the photocatalytic-reduction-application of Cu^{II} /NA-PVA composite.

3.7. Photocatalytic Activity

Figure 7 shows the UV–vis absorption spectra of the IC dye solutions irradiated by UV light in the presence of Cu^{II} /NA-PVA catalyst. IC itself, in the absence of a catalyst, was photochemically inert (blank), as pointed out by no change in the absorption spectrum. The maximum wavelength for IC dye was determined to be 608 nm. This peak accounts for the blue color of solutions and can be attributed to the $n \rightarrow \pi^*$ (transition of the non-bonding electrons to the anti-bonding π) group orbital of the double-bond system, and it was used to monitor the mineralization of the dye. Increasing the mineralization efficiency of IC on Cu^{II} /NA-PVA is accounted for oxidative degradation of the dye.

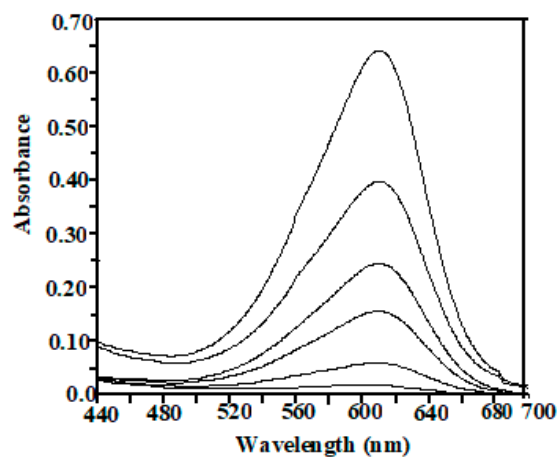


Figure 7. The time-resolved absorption spectra during the reaction of 100 ppm of IC in the presence of 100 mg Cu^{II} /NA-PVA catalyst under UV illumination. Decreasing absorbance of the bands for IC is related to 0.0 to 60 min from up to down.

The calculated amount of CO_2 evolved from the reaction that was captured by an aqueous solution of barium hydroxide and determined gravimetrically, as precipitated barium carbonate measured 55% of the dye carbon atoms, calculated theoretically. The sulphate ions, on the other hand, determined as barium sulphate using barium chloride solution, measured a lower value than expected, based on stoichiometric ratios; this is possibly due to the adsorption of some sulphate ions on the catalyst surface. These results indicate that the oxidative degradation of IC on Cu^{II} /NA-PVA can be proposed.

The photocatalytic-reactions of indigo carmine on NA-PVA, Ni^{II} - & Cu^{II} /NA-PVA were carried out in order to evaluate the activities of the prepared photocatalysts. No

significant decolorization IC dyes were detected through stirring the solution contaminated with dye and with a catalyst for over 120 min. This obviously designated the activity of the photocatalytic as a catalyst without any adsorption of the dye over copolymers. Blank experiments were carried out in the absence of a catalyst, in the presence of the copolymer with H_2O_2 and UV irradiation (about 77.7% degradation was noticed over 60 min) (Figure 8). The photocatalytic activities of indigo carmine were observed with the presence of Ni^{II} /NA-PVA and Cu^{II} /NA-PVA; approximately 93.7% degradation was detected with Cu^{II} -chelates after 35 min. As shown in Figure 8, the absorption of indigo carmine solution was observably decreased just after the beginning of visible light-irradiation, when Cu^{II} /NA-PVA was used as the photocatalyst. Increasing of the light-irradiation time results in a further decrease in the absorption. Conversely, a decrease in the photocatalytic activity of the catalyst was detected on complexation with Ni^{II} /PVA-NA. Nearly 75% conversion was obtained after 35 min and approximately 90% after 60 min.

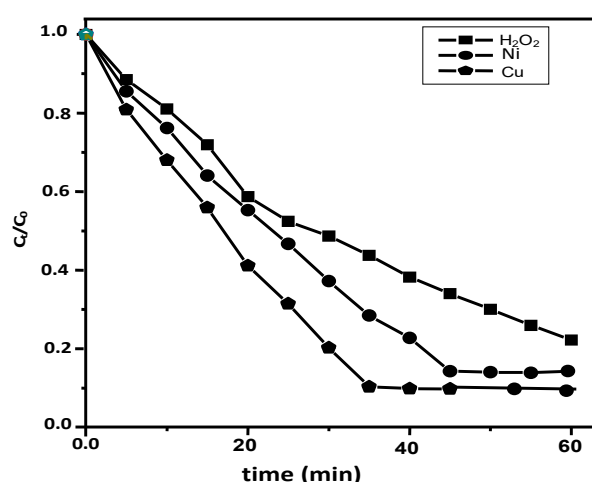


Figure 8. The change in the decolorization of IC over time for photocatalytic degradation by NA-PVA, Cu^{II} /NA-PVA and Ni^{II} /NA-PVA samples. Experimental condition: pH 2, $T = 25^\circ C$, catalyst mass = 100 mg, volume = 200 mL, and initial dye conc. 100 ppm.

The kinetics of de-coloration by immersion in C_0/C_t was plotted vs. t (min), which designates straight lines, where the slopes indicate the factors of the reaction rate. It can be clearly seen that the Cu^{II} /PVA-NA has a better photocatalytic property than Ni^{II} /PVA-NA. These lines indicate that this degradation reaction mimics the 1st kinetic-reaction with $k = 0.03 \text{ min}^{-1}$ and $R^2 = 0.988$. From the experimental data, we can conclude that the increasing rate of the degradation for Cu^{II} /PVA-NA relevant to reduced BG with high dispersion (showed in XRD).

3.8. Molecular Modeling Studies

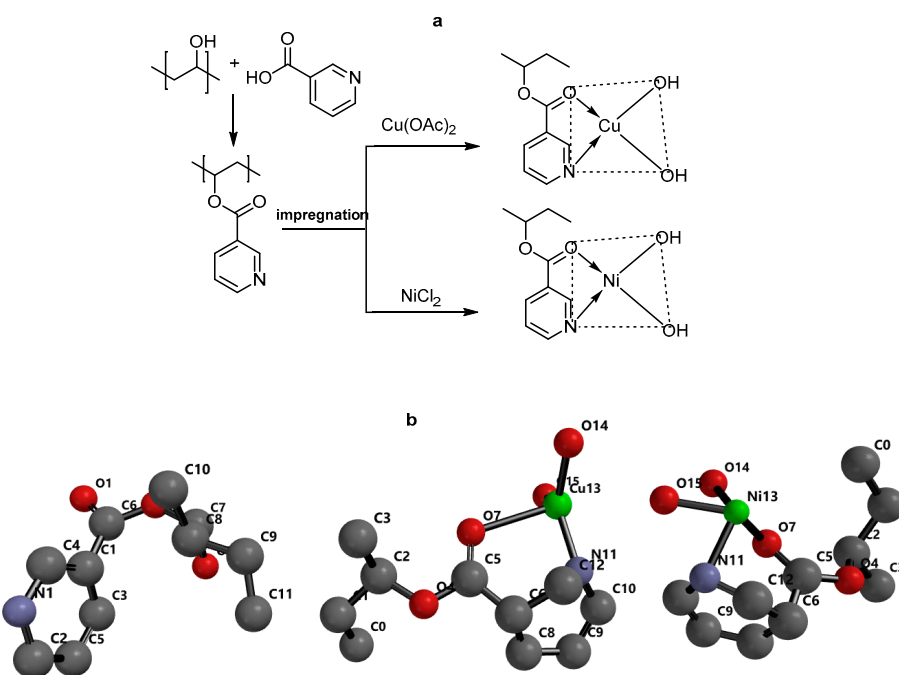
3.8.1. Molecular Geometry

The optimization geometry was performed using DFT molecular orbital, as reported earlier [49]. All calculated energies are listed in (Table 3). The pyridine ring was arranged in parallel mode with the aliphatic chain to stabilize the PVA-NA. The pyridine as well as M-core for Cu^{II} & Ni^{II} copolymers were stabilized in coplanar arrangement with an aliphatic chain, which confirming by the tetrahedral angle (10.25°) between (C1-C2-C5-C6), as represented in (Scheme 1). The C6=O1 of PVA-NA indicates ($1.219^\circ A$) length, with the lengths for C5=O7 reducing due to their bonding with metals, demonstrated as 2.485 and $1.809^\circ A$, respectively. Furthermore, the modern M-ring displayed N11-M($1.929, 1.964$), O7-M($1.840, 1.797^\circ A$) over Cu^{II} & Ni^{II} copolymers, respectively. The angle for (C6-C8-C5) bond for ligand displayed (30.97°), while Cu^{II} & Ni^{II} copolymers showed N11-M-O (84.75 and 30.6) and M13-O14-O15 ($84.44, 57.43^\circ$), respectively.

Table 3. Calculated energetic of reactivity parameters for compounds PVE and M^{II}/PVE at DFT with a B3LYP/6-31G* Basics sets.

Cpd.	PVE	Cu	Ni	Cpd.	PVE	Cu	Ni
E	-475.22	-460.67	-1190.71	Ω_i	5.47	2.95	2.02
HOMO	-10.41	-3.72	-3.58	μ^+	-2.99	-2.56	-1.24
LUMO	-0.52	-2.17	-0.46	μ^-	-7.94	-3.33	-2.80
ΔG	-9.89	-1.55	-3.12	Ω^-	6.37	7.16	2.51
I	10.41	3.72	3.58	Ω^+	2.40	5.50	1.11
A	0.52	2.17	0.46	Ω^\pm	8.77	12.66	3.63
η	4.95	0.78	1.56	ΔN_{max}	-0.55	-1.90	-0.65
S	0.20	1.29	0.64	$\Delta\rho_{KNU}$	14.80	-39.25	14.80
χ	-5.47	-2.95	-2.02	$\Delta\rho_{KELE}$	1.98	-2.58	1.98

E: energy (kcal/mol), HOMO: Highest Occupied Molecular Orbital (eV), LUMO: Lowest Occupied Molecular Orbital (eV), ΔG : energy Gap (eV), I: Ionization potential, A: electron affinity; H: Hardness (eV), S: Softness (eV), X: Electronegativity (eV), Ω_i : electrophilicity index; μ^+ : electron accepting ability, μ^- : electron donating ability, Ω^+ : electrophile power (electron accepting capacity), Ω^- : Nucleophilicity power (electron donating capacity); Ω^\pm : nucleophilicity (eV); ΔN_{MAX} : maximum number of electrons transfer in ground state. $\Delta\rho_{KELE}$ Group electrophilicity; $\Delta\rho_{KNU}$: Group nucleophilicity.

**Scheme 1.** (a) Synthesis of PVNE ligand and its complexes. (b) Optimization geometry of ligand and their metal complexes, which were represented in the numbering ball and stick model, the hydrogen atoms removed for clarifying.

3.8.2. Stability Inter- and Intra-Molecular Interaction Stability

(i) Chemical Reactivity & Frontier orbital analysis

We studied frontier molecular orbitals (FMOs), which play an important role in understanding the way the tested compounds interact with different chemical systems. FMOs' gap has been calculated to determine the chemical reactivity and kinetic stability of the molecule. The chemical interaction was stabilized inversely with the energy gap.

Stabilization interaction was improved by increasing E_{HOMO} for one molecule and decreasing E_{LUMO} energy in another [50]. The E_{HOMO} and E_{LUMO} have been estimated using DFT theory and are listed in Table 3 [51]. The increasing of the E_{HOMO} indicated the elevated power of the practical in donating electron direction, which is related to detached electrons from the valance shell, exhibiting a high ability via oxidation, and vice versa [50,52]. The E_{HOMO} for the ligand was exhibited at a higher value than its

metal complexes, while the values for both Cu and Ni complexes were nearly the same. The HOMO region condensed PVA-NA over C=O of pyridine moiety (Figure 9). The HOMO in the case of Cu^{II}-/Ni^{II}- chelates is located in pyridine and metal rings (Figure 9). Furthermore, the LUMO zone condensed over the pyridine ring for PVA-NA and Ni-chalet. While, in Cu-complex, LUMO zone was situated on the pyridine and metal rings (Figure 9).

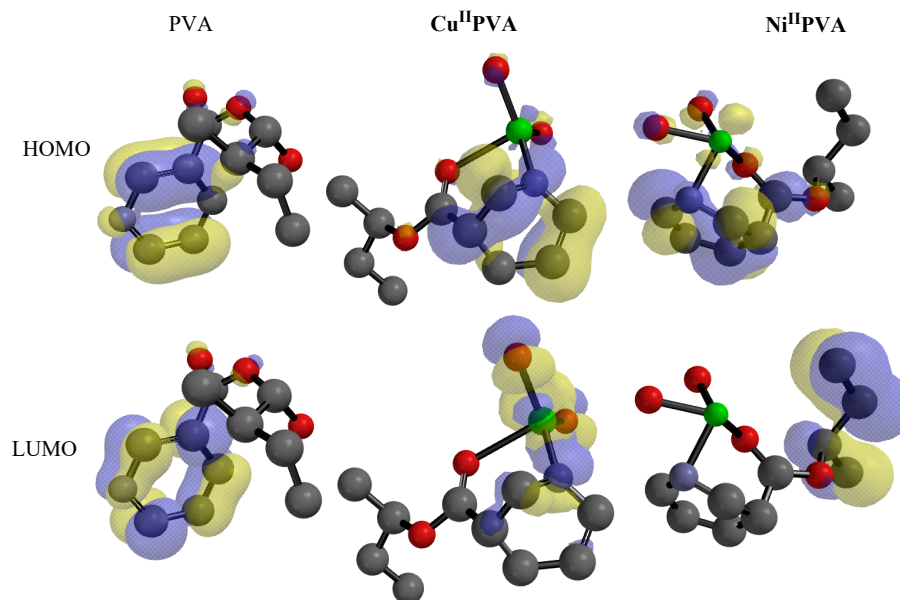


Figure 9. Frontier molecular orbitals (HOMO and LUMO) for PVE, Ni/PVA-NA and Cu/PVA-NA at DFT/BY3LP.

E_{HOMO} s and E_{LUMO} s for the PVA-NA and M/PVA-NA have negative values. These values promote the high stability interaction with the dye, and migration of electrons from the aliphatic chain to pyridine and metal rings through an intramolecular transfer mechanism. In addition, FMOs are directly linked via softness and hardness. Thus, one can interpret the electrophiles and nucleophiles through these concepts. PVA-NA and M/PVA-NA exhibited low ΔG values, organized as *ligand* < Ni^{II} < Cu^{II} and demonstrated that: (i) an elevated chemical reactivity, (ii) growing softness and trended as $PVE < Ni^{II} < Cu^{II}$, (iii) The nucleophilicity increasing as $Cu^{II} < PVE < Ni^{II}$. While, PVE was presented the highest on the electrophilicity index ($\omega_1 = 5.47$ ev.), which easily explained the complexation with metal ions. The highest electron accepting ability “ μ^+ ” appeared in NA-PVA. Electron donating chemical potential increased by introducing Cu^{II} over original polymer and Ni^{II} ion. Intermolecular reactivity has been analyzed founded on group-philicity “ ω^\pm ”. This term is used when electrophile and nucleophile is hitting simultaneously for particles. The positive value of ω^\pm has been attributed to likely electrophile attacking with ($\omega^- < \omega^+$) and charge shift as media \rightarrow molecule, and vice versa. The ω^\pm for ligand and copolymers have a positive value arranged as $Cu^{II} < PVA-NA < Ni^{II}$, thus, the nucleophilicity is more likely for tested compounds. From (Table 3) one can deduce that these ligand and copolymers are promising nucleophiles with high ability for receiving electrons from dye ($\omega^- = 2.51\text{--}6.37\text{ev.}$). In addition, ΔN_{max} has -Ve values between -0.55 and -1.95 ev. and the electron cloud migrates as Ligand \rightarrow Dye (Table 3)

(ii) Molecular electrostatic potential map (EPM)

The electrostatic potential map (EPM) can identify dye by the equilibrium between repulsive (+charge) and attractive (-charge) forces [53], and is related to nucleophilic electrophilic reactivities, respectively. The EPM was mapped for ligand and metal complexes (Figure 10). The areas with high electron density were highlighted (orange, yellow, red). The positive efficiency region has colors toward blue, while the intermediate potential

region is shaded by the color green. The positive charge was enclosed over pyridine in NA-PVA and CuII copolymer, while in Ni complex, +Ve tagged upon the metal ring. The difference between colors in EPM morphology demonstrated the electrostatic variation between potential values. Growth in the red zone for all compounds under investigation indicated the high ability of electrophilic process responsible to recognize the nucleophile groups in the dye.

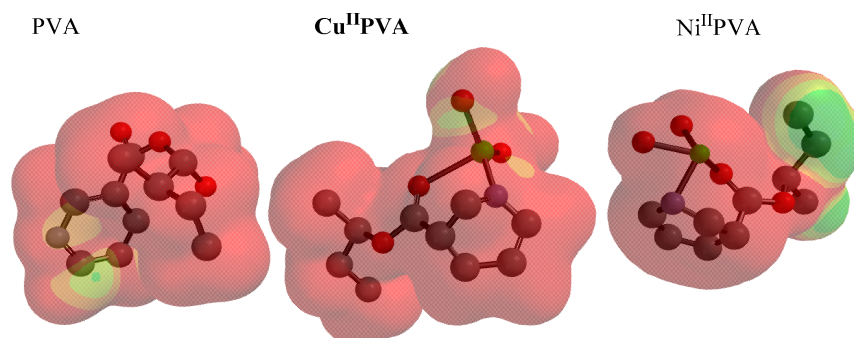


Figure 10. Electrostatic potential for PVE, Ni/PVA-NA and Cu/PVA-NA at DFT/BY3LP.

(iii) The Local Reactivity profile

The local reactivity (LR) parameters were identified by the variation in electronic systems, through distortion on the electronic cloud at the exact atomic region related to accepting or donating of electrons [54,55]. LRs were accomplished at examining site-selectivity toward chemical reaction (Figure 11).

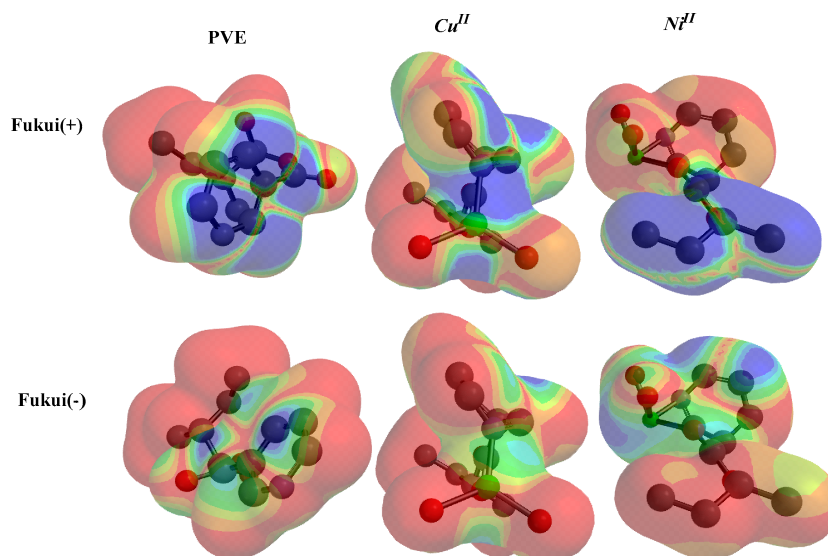


Figure 11. Fukui-function (electrophile and nucleophile) for PVE, Ni/PVA-NA and Cu/PVA-NA using DFT/BY3LP.

The " f_k^+ ", signified by the red color corner, displayed the rise in electron density after gaining charge, while +Ve was represented by the blue color. In " f_k^- ", the red site revealed reducing electron density after donating electrons. In PVA-NA, the C=O group has the most sensitive site against earning or contributing electrons (" f_k^- and f_k^+ "). This observation showed that the electron cloud migrated between the pyridine ring and C=O, which caused the stabilization interaction with metal. The negative charges in Cu^{II}, Ni^{II} copolymers are more condensed over M-cores for both cases f_k^- and f_k^+ , thus, the electron departed as pyridine \rightarrow M-cores and enhanced the chelation power with dye.

The variation in the density of charges where electrons were gained in the electronic system from dye “D” atom was represented by “ $\Delta\rho_{KElec}$ ”. When this mechanism is reversed, it can be represented as “ $\Delta\rho_{KNuc}$ ”.

$$\Delta\rho_D^{Elec} = -\left(\frac{\mu^+}{\eta}\right)^2 + 1/2\left(\frac{\mu^+}{\eta}\right)^2 (f_k^+ - f_k^-) \quad (2)$$

$$\Delta\rho_D^{Nuc} = -\left(\frac{\mu^\pm}{\eta}\right)^2 + 1/2\left(\frac{\mu^\pm}{\eta}\right)^2 (f_k^+ - f_k^-) \quad (3)$$

3.8.3. Hirshfeld Fingerprint

Hirshfeld fingerprint surface (HF) was utilized for examining the intermolecular interaction between neighbor molecular sites. The HF for the polymer and its complexes has been explained by “ d_{norm} , d_e & d_i ” terms, which are related to the interior or exterior distance between neighbor atomic sites, respectively (Figure 12). The d_{norm} was calculated using the following Equation (4) [10]:

$$d_{norm} = (d_i - r^{vdW}_i)/r^{vdW}_i + (d_e - r^{vdW}_e)/r^{vdW}_e \quad (4)$$

where r^{vdW}_i and r^{vdW}_e are Van der Waals radii for the internal and external of the closest atomic site via the molecular surface.

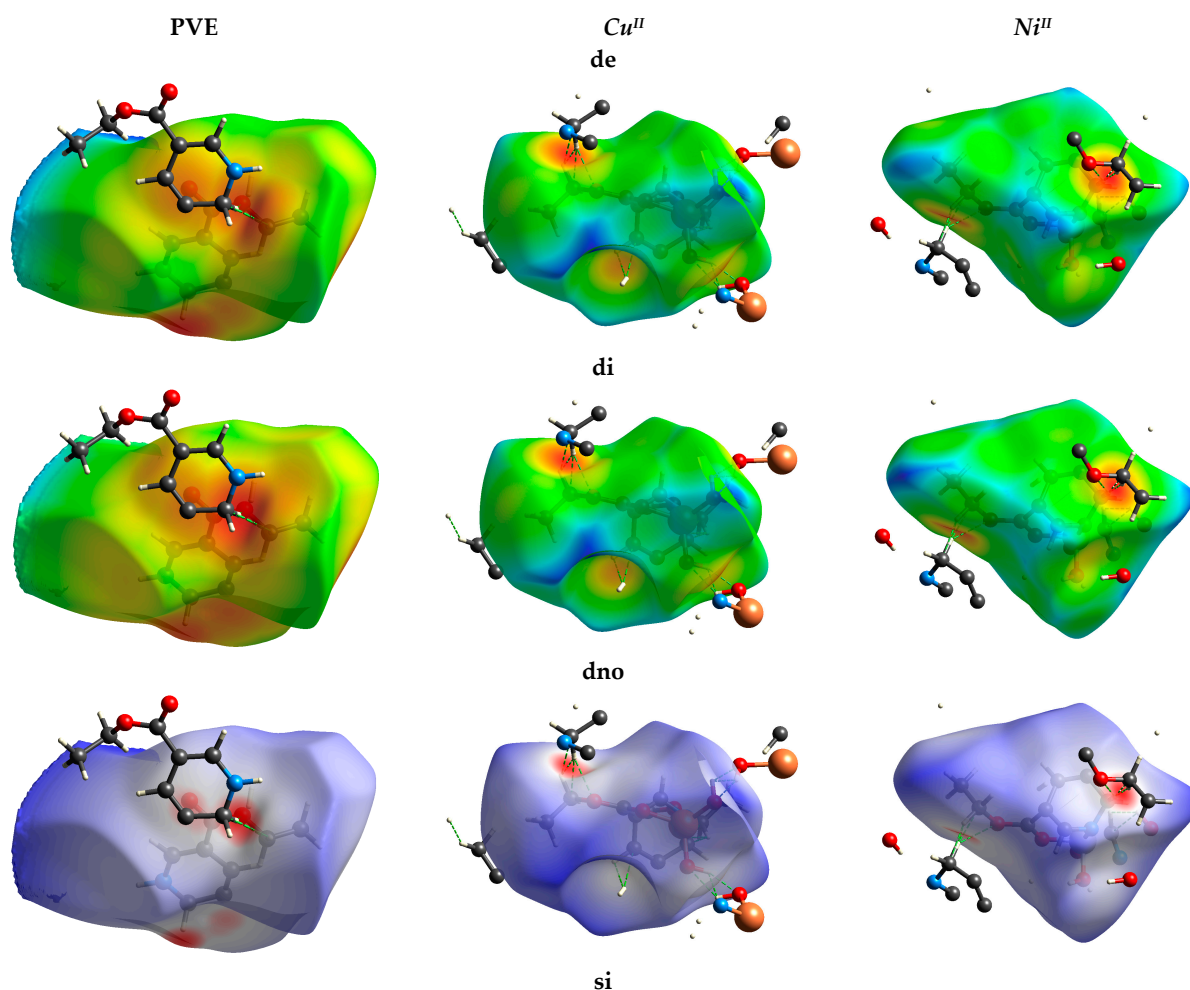


Figure 12. Cont.

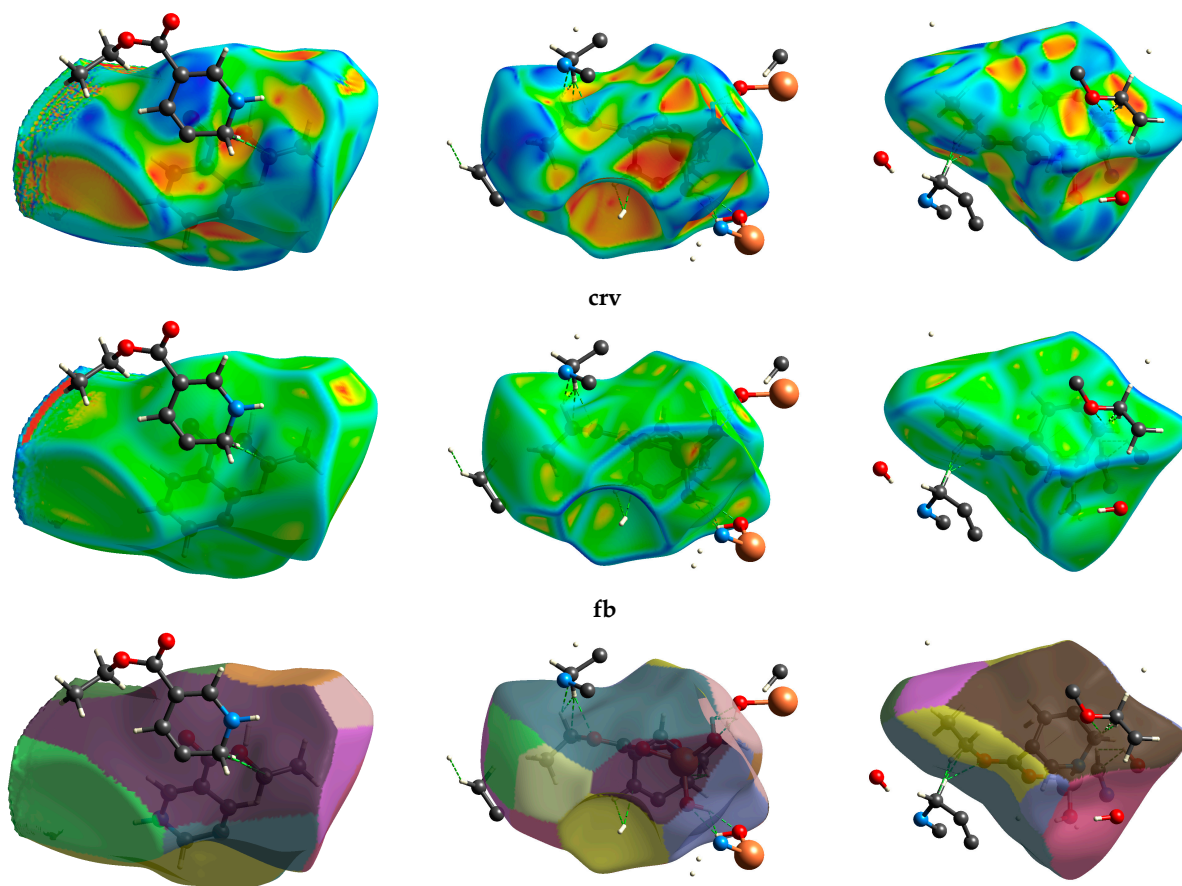


Figure 12. Molecular Hirshfeld fingerprints d_{norm} , d_i , d_e , shape index “ si ” and curvedness “ crv ”, and fragment batch “ fb ” in compound **2a,b**.

If d_{norm} has a positive value, it means r^{vdW} is short, while long r^{vdW} has a negative value. The 3D HS of ligand showed $d_{norm} = -0.7823$ to 6.6325 Å, $d_i = 0.6105$ to 6.3480 Å, $d_e = 0.6085$ – 7.4791 Å, shape-index = -1.00 to 1.00 Å, curvedness = -4.00 to 4.00 Å, and patch fragment = 0.00 – 12.00 Å, respectively. While HFs for Cu^{III} & Ni^{III} complexes represented $d_i = (0.6052$ – $3.9391)$; $(0.4807$ – $3.7731)$ Å; $d_e = (0.6062$ – $3.7924)$; $(0.4795$ – $3.7785)$ Å; $d_{norm} = (-0.8477$ – $3.6947)$; $(-1.1191$ – $3.6686)$ Å; $SI = -1.0000$ – 1.0000 , $Crv. = (-4.0000$ – $4.0000)$ Å, $BF = 0.0000$ – 15.0000 Å, respectively. The intermolecular interactions were contributed in ligand lattice as (C ... H/H ... C; 8.8%), (C ... O/O ... C; 3.7%), (O ... H/H ... O; 14.3%), respectively. The Cu^{III} showed (O ... H/H ... O; 30.1%), (C ... H/H ... C; 9.1%), (C ... O/O ... C; 4.6%). The Nickel complex showed (O ... H/H ... O; 19.6%), (C ... H/H ... C; 10.6%), (C ... O/O ... C; 4.3%), (N ... O/O ... O; 1.4%). The d_{norm} illustrated that the weak O ... H/H ... OH binding represented with light blue shading, which contributed to the molecular structure of the Cu^{III} polymer more than Ni^{III} and PVE. The C ... O/O ... C interactions appeared as a green spike in di HF (Figure 12). The low degree of curvedness in HF in all structures was due to the flat surface sites in all particles. The curvature sites are sharp due to the sharp curvedness degree. The surface was divided two folds, which comes back to the bonding between the closest particles. The concave zones located in the curvedness indicated the presence of weak stacking π ... π interactions (red greenish concave).

3.8.4. Nonlinear Optical Effects

Linear and nonlinear optical characteristics were estimated for PVA-NA, CuII, and NiII-copolymers: μ :dipole moments “determines electrostatic interaction power against media”; α : polarizability “related to deformation level for density of electron, depending

on morphological and bonding nature of particles". Furthermore, the following parameters (" α_0 " mean polarizability, " $\Delta\alpha$ " anisotropic polarizability and " β_0 " first order hyperpolarizability) have been estimated vis (x, y & z) tensors of polarizability [56].

Urea has been used as a standard NLO material with μ (1.3732 Debye) and β_0 (0.3728×10^{-30} esu.) [57]. The PVA-NA, CuII, and NiII-copolymers possess good NLO properties when compared to the standard material (Urea; $\mu = 1.3732$ Debye $\beta_0 = 0.3728 \times 10^{-30}$ esu.) [57].

The hyperpolarizability was demonstrated in trend as CuII > NiII > urea > PVE-NA, as represented in (Table 4). The increase in this characteristic related to the existence of conjugation π -electron systems. Furthermore, we used the reversal relation between ΔG and hyperpolarizability to explain the NLO's characteristic. The energy gap for ligand and related copolymers has negative values; this implies a significant, non-direct relationship with their optical characteristics [58]. This information upheld the intramolecular charge transfer (donating \rightarrow accepting) electron through π -electron systems [59].

Table 4. Calculated thermodynamic parameters for compounds PVE and MII/PVE at DFT with a B3LYP/6-31G* basics sets. Schemes follow the same formatting.

Cpd.	PVE	Cu	Ni	Cpd.	PVE	Cu	Ni
ZPE	210.474	632	173.62	First order hyperpolarizability (β)			
G°	26.940	31.00	24.54	β_{xxx}	43.275	414.85	−434.3
S°	155.573	187.1	143.29	β_{xyy}	−21.683	637.40	108.3
C _V °	137.541	173.82	122.90	β_{xzz}	3.107	−32.98	−273.3
Dipole moment (μ)				β_{yyy}	73.202	−1326.10	−591.8
μ_x	0.837	−2.215	5.167	β_{xxy}	−5.484	−178.39	−173.0
μ_y	−1.050	−1.880	−0.819	β_{yzz}	5.606	35.62	181.1
μ_z	0.676	0.228	0.242	β_{zzz}	−20.301	−276.35	−154.6
μ	3.820	7.408	13.311	β_{xyz}	−5.203	132.43	341.6
Polarizability (α)				β_{yyz}	−9.152	638.36	−434.3
α_{xx}	90.894	151.622	204.1126	β_0	−0.275	2.618	−18.177
α_{yy}	105.193	167.854	205.3385				
α_{zz}	96.175	156.137	119.0984				
α_{xz}	18.405	−29.312	−22.04				
α_{xy}	3.145	11.501	−7.19				
α_{yz}	−3.406	12.729	−25.99				
α_0	2.887	4.698	5.22				
$\Delta\alpha$	9.79	40.22	43.83				

ZPE: zero-point vibrational energies (kJ/mol), H°: Enthalpy (kJ/mol), G°: Gibbs free energy (kJ/mol), S°: Entropy (kJ/mol), C_V°: Constant volume molar heat capacity, μ : dipole moment (Debye), α_0 : mean polarizability ($\times 10^{-30}$ esu), $\Delta\alpha$: anisotropic polarizability ($\times 10^{-30}$ esu), β : hyperpolarizability ($\times 10^{-30}$ esu) may have a footer.

4. Conclusions

- PVA was successfully modified with nicotinic acid, yielding graft copolymers.
- FT-IR and NMR spectroscopy confirmed the distribution of NA onto PVA, and the coordinating of copolymer with the M-ion.
- The ESR spectra showed the distorted square planar structure in Ni^{II}/PVA-NA and Cu^{II}/PVA-NA complexes.
- Incorporation of Ni^{II} and Cu^{II} into PVA-NA plays an advantageous role in the thermal stability through ionic interaction. Thus, the Ni^{II} and Cu^{II} copolymers become better blending agents than PVA-NA itself.
- The adsorption of IC dye onto Cu^{II}/NA-PVA complex was noticeably greater (90%) in 35 min.
- The simulated FMOs showed that the ligand and copolymers are promising nucleophiles with high ability for receiving electrons from dye is related to the distribution

of M-ions into PVA-NA; this occurs due to electron transfer between aliphatic chain of PVA-NA and *M-core*.

- The EPMs showed that the electrophilic site for these copolymers recognized the nucleophile region of the dye.
- The ΔN_{max} for copolymers demonstrated that the charge migrates as Ligand \rightarrow Dye.
- NLO studies introduce a clear picture of promising optical properties compared to standard material.

Supplementary Materials: The following are available online at <https://www.mdpi.com/article/10.3390/cryst11101244/s1>, Materials and Methods.

Author Contributions: Conceptualization, I.O.A. and A.A.E.; methodology, H.S.N.; software, A.A.E.; validation, I.O.A., L.M.A.-H. and A.A.E.; formal analysis, A.M.N.; investigation, I.O.A.; resources, A.M.N.; data curation, H.S.N.; writing—original draft preparation, I.O.A., A.A.E.; writing—review and editing, I.O.A., A.A.E.; visualization, I.O.A.; supervision, I.O.A. All authors have read and agreed to the published version of the manuscript.

Funding: This work was funded by the Deanship of Scientific Research, King Saud University through vice Deanship of Scientific Research Chairs.

Institutional Review Board Statement: The study did not involve humans.

Informed Consent Statement: The study did not involve humans.

Data Availability Statement: Samples of the compounds are available from Ahmed A. Elhenawy.

Conflicts of Interest: The authors declare no conflict of interest.

References

1. Klaus, H. *Industrial Dyes-Chemistry, Properties, Applications*; Wiley-VCH: Weinheim, Germany, 2003.
2. Dąbrowski, A. Adsorption—from theory to practice. *Adv. Colloid Interf. Sci.* **2001**, *93*, 135–244. [[CrossRef](#)]
3. Reife, A. Dyes, environmental chemistry. In *Kirk-Othmer Encyclopedia of Chemical Technology*; John Wiley & Sons: Hoboken, NJ, USA, 2000.
4. Olness, A. Water Quality: Prevention, Identification and Management of Diffuse Pollution. *J. Environ. Qual.* **1995**, *24*, 383. [[CrossRef](#)]
5. Zollinger, H. *Color Chemistry: Synthesis, Properties and Applications of Organic Dyes and Pigments*, 2nd ed.; VCH Publisher: New York, NY, USA, 1991.
6. Cang-Rong, J.T.; Pastorin, G. The influence of carbon nanotubes on enzyme activity and structure: Investigation of different immobilization procedures through enzyme kinetics and circular dichroism studies. *Nanotechnology* **2009**, *20*, 255102. [[CrossRef](#)]
7. Golder, A.K.; Samanta, A.N.; Ray, S. Anionic reactive dye removal from aqueous solution using a new adsorbent—Sludge generated in removal of heavy metal by electrocoagulation. *Chem. Eng. J.* **2006**, *122*, 107–115. [[CrossRef](#)]
8. Zhang, S.F.; Xiong, F.; He, Z.; Liang, Y.; Xue, J.R.; Jing, L.H.; Qin, D.B. Syntheses, structures, luminescent and gas adsorption properties of five new interpenetrated, 2D and 3D metal–organic frameworks based on a semi-rigid bis (imidazole)-carbazole ligand. *Polyhedron* **2015**, *102*, 401. [[CrossRef](#)]
9. Wang, F.; Wang, C.; Yu, Z.; Xu, K.; Li, X.; Fu, Y. Two multifunctional Mn (II) metal–organic frameworks: Synthesis, structures and applications as photocatalysis and luminescent sensor. *Polyhedron* **2016**, *105*, 49. [[CrossRef](#)]
10. Xie, W.F.; Guo, L.Y.; Xu, J.H.; Jagodič, M.; Jagličić, Z.; Wang, W.G.; Zhuang, G.L.; Wang, Z.; Tung, C.H.; Sun, D. Multifaceted bicubane Co₄ clusters: Magnetism, photocatalytic oxygen evolution, and electrical conductivity. *Eur. J. Inorg. Chem.* **2016**, *20*, 3253. [[CrossRef](#)]
11. Yan, Z.H.; Li, X.Y.; Liu, L.W.; Yu, S.Q.; Wang, X.P.; Sun, D. Single-crystal to single-crystal phase transition and segmented thermochromic luminescence in a dynamic 3D interpenetrated AgI coordination network. *Inorg. Chem.* **2016**, *55*, 1096. [[CrossRef](#)] [[PubMed](#)]
12. Kaliyappan, T.; Kannan, P. Co-ordination polymers. *Prog. Polym. Sci.* **2000**, *25*, 343–370. [[CrossRef](#)]
13. Hu, T.; Wang, X.; Xue, Z.; Zhang, X.; Wang, X. Structural control and magnetic properties of three Co (II) coordination polymers based on 6-(3, 5-dicarboxylphenyl) nicotinic acid. *Polyhedron* **2017**, *127*, 449–457. [[CrossRef](#)]
14. Lim, M.; Kwon, H.; Kim, D.; Seo, J.; Han, H.; Khan, S.B. Highly-enhanced water resistant and oxygen barrier properties of cross-linked poly (vinyl alcohol) hybrid films for packaging applications. *Prog. Org. Coat.* **2015**, *85*, 68–75. [[CrossRef](#)]
15. Carlotti, S.J.; Giani-Beaune, O.; Schué, F. Characterization and mechanical properties of water-soluble poly (vinyl alcohol) grafted with lactic acid and glycolic acid. *J. Appl. Polym. Sci.* **2001**, *80*, 142–147. [[CrossRef](#)]
16. Son, B.; Yeom, B.Y.; Song, S.H.; Lee, C.S.; Hwang, T.S. Antibacterial electrospun chitosan/poly (vinyl alcohol) nanofibers containing silver nitrate and titanium dioxide. *J. Appl. Polym. Sci.* **2008**, *111*, 2892–2899. [[CrossRef](#)]

17. Hnatejko, Z.; Dutkiewicz, G.; Kubicki, M.; Lis, S. New complexes of cobalt (II) ions with pyridinecarboxylic acid N-oxides and 4, 4'-byp. *J. Mol. Struct.* **2013**, *1034*, 128–133. [[CrossRef](#)]
18. Marandi, F.; Moeini, K.; Ghasemzadeh, S.; Mardani, Z.; Quah, C.K.; Loh, W.S. Synthesis, spectral and X-ray diffraction of two new 2D lead (II) coordination polymers formed by nicotinic acid N-oxide linkers. *J. Mol. Struct.* **2017**, *1149*, 92–98. [[CrossRef](#)]
19. Marandi, F.; Quah, C.K.; Hoong-Kun, F. The first crystal structures of two 2-D lead (II)-coordination polymers with picolinic acid N-oxide and pseudohalides extended to 3-D networks by intermolecular interactions. *J. Coord. Chem.* **2013**, *66*, 986–994. [[CrossRef](#)]
20. Singh, R.; Rao, R.S.S. Synthesis and characterization of divalent manganese, cobalt, nickel, copper and zinc complexes with nicotinic acid. *J. Mol. Struct.* **1981**, *71*, 23–30. [[CrossRef](#)]
21. Gimenez, V.; Mantecon, A.; Ronda, J.C.; Cadiz, V. Poly (vinyl alcohol) modified with carboxylic acid anhydrides: Crosslinking through carboxylic groups. *Appl. Polym. Sci.* **1997**, *65*, 1643–1651. [[CrossRef](#)]
22. Şenel, M.; Bozkurt, A.; Baykal, A. An investigation of the proton conductivities of hydrated poly (vinyl alcohol)/boric acid complex electrolytes. *Ionics* **2007**, *13*, 263. [[CrossRef](#)]
23. Serna, C.; Fornes, V.; Fernandez-Navarro, J.M. Sol gel transition in simple Silisate. *J. Non-Cryst. Solids* **1984**, *63*, 45.
24. Patel, R.N.; Gundla, V.L.N.; Patel, D.K. Synthesis, characterization and properties of some ternary copper (II) complexes containing NOS donor Schiff base and NN donor bidentate ligands. *Indian J. Chem.* **2008**, *47*, 353.
25. Lever, A. *Inorganic Electronic Spectroscopy*, 2nd ed.; Elsevier: Amsterdam, The Netherlands, 1984.
26. Singh, O.I.; Damayanti, M.; Singh, N.R.; Singh, R.H.; Mohapatra, M.; Kadam, R.M. Synthesis, EPR and biological activities of bis (1-n-butylamidino-O-alkylurea) copper (II) chloride complexes: EPR evidence for binuclear complexes in frozen DMF solution. *Polyhedron* **2005**, *24*, 909–916. [[CrossRef](#)]
27. El-Boraey, H.; Abdel-Rahman, R.; Atia, E.; Hilmy, K. Spectroscopic, thermal and toxicity studies of some 2-amino—3-cyano—1, 5-diphenylpyrrole containing Schiff bases copper (II) complexes. *Open Chem.* **2010**, *8*, 820–833. [[CrossRef](#)]
28. Raman, N.; Jeyamurugan, R.; Subbulakshmi, M.; Boominathan, R.; Yuvarajan, C.R. Synthesis, DNA binding, and antimicrobial studies of novel metal complexes containing a pyrazolone derivative Schiff base. *Chem. Pap.* **2010**, *64*, 318–328. [[CrossRef](#)]
29. Pai, S.; Newalkar, B.; Choudary, N. Synthesis and characterization of cobalt substituted aluminophosphate molecular sieve: Co-SSZ-51 under microwave-hydrothermal conditions. *Microporous Mesoporous Mater.* **2006**, *96*, 135. [[CrossRef](#)]
30. Duan, F.; Chen, J.P.; Yu, J.; Xu, R. A low-cost route to the syntheses of microporous cobalt-substituted aluminophosphates by using the waste mother-liquor. *Microporous Mesoporous Mater.* **2009**, *126*, 26. [[CrossRef](#)]
31. Coats, A.; Redfern, J. Kinetic parameters from Thermogravimetric data. *Nature* **1964**, *201*, 68–69. [[CrossRef](#)]
32. Horowitz, H.; Metzger, G. A new analysis of thermogravimetric traces. *Anal. Chem.* **1963**, *35*, 1464. [[CrossRef](#)]
33. Frost, A.; Pearson, R. *Kinetics and Mech.*, 2nd ed.; Wiley: New York, NY, USA, 1961; p. 88.
34. Othman, I. Sol-gel synthesis of NiFe₂O₄ with PVA matrices and their catalytic activities for one-step hydroxylation of benzene into phenol. *J. Therm. Anal. Calorim.* **2014**, *116*, 805.
35. Maravalli, P.; Goudar, T. Thermal and spectral studies of 3-N-methyl-morpholino-4-amino-5-mercapto-1, 2, 4-triazole and 3-N-methyl-piperidino-4-amino-5-mercapto-1, 2, 4-triazole complexes of cobalt (II), nickel (II) and copper (II). *Thermochim. Acta* **1999**, *325*, 35. [[CrossRef](#)]
36. Yusuff, K.; Sreekala, R. Thermal and spectral studies of 1-benzyl-2-phenylbenzimidazole complexes of cobalt (II). *Thermochim. Acta* **1990**, *159*, 357. [[CrossRef](#)]
37. Mohamed, G.; Abd El-Wahab, Z. Salisaldehyde-2-aminobenzimidazole schiff base complexes of Fe (III), Co (II), Ni (II), Cu (II), Zn (II) and Cd (II). *J. Therm. Anal. Calorim.* **2003**, *73*, 347–359. [[CrossRef](#)]
38. Bhaskare, C.; Hankare, P. Cobalt-, Nickel- and Copper (II) Complexes of Schiff Bases with N or S Donor Sites. *J. Ind. Chem. Soc.* **1995**, *72*, 585.
39. Donia, A.; Gouda, M.; Ayad, M.; El-Boraey, H. Synthesis and thermal characterization of new ternary chelates of piroxicam and tenoxicam with glycine and dl-phenylalanine and some transition metals. *Thermochim. Acta* **1992**, *194*, 155. [[CrossRef](#)]
40. Kulkarni, S.; Kittur, A.; Aralaguppi, M.; Kariduraganavar, M. Synthesis and characterization of hybrid membranes using poly (vinyl alcohol) and tetraethylorthosilicate for the pervaporation separation of water–isopropanol mixtures. *J. Appl. Polym. Sci.* **2004**, *94*, 1304. [[CrossRef](#)]
41. Isiklan, N.; Sanli, O. Separation characteristics of acetic acid–water mixtures by pervaporation using poly (vinyl alcohol) membranes modified with malic acid. *Chem. Eng. Process.* **2005**, *44*, 1019. [[CrossRef](#)]
42. Wang, S.F.; Gu, F.; Lü, M.K.; Cheng, X.F.; Zou, W.G.; Zhou, G.J.; Wang, S.M.; Zhou, Y.Y. Synthesis and photoluminescence characteristics of Dy³⁺-doped ZnAl₂O₄ nanocrystals via a combustion process. *J. Alloys Compd.* **2005**, *394*, 255–258. [[CrossRef](#)]
43. Bai, H.; Liu, Z.; Sun, D. Catalytic partial oxidation of isobutanol for the production of hydrogen. *Int. J. Hydrogen Energy* **2012**, *37*, 1399.
44. Kislova, N.; Srinivasana, S.; Emirov, Y.; Stefanakos, E. Optical absorption red and blue shifts in ZnFe₂O₄ nanoparticles. *Mater. Sci. Eng. B* **2008**, *153*, 70–77. [[CrossRef](#)]
45. Saha, B.; Das, S.; Chattopadhyay, K. Electrical and optical properties of Al doped cadmium oxide thin films deposited by radio frequency magnetron sputtering. *Sol. Energy Mater. Sol. Cells* **2007**, *91*, 311. [[CrossRef](#)]
46. Fan, W. A Novel Carbon Nanotube Structure Formed in Ultra-Long Nanochannels of Anodic Aluminum Oxide Templates. *J. Phys. Chem. B* **2006**, *110*, 2080.

47. Manikandan, A.; Durka, M.; Arul, S. Preparation and characterization of nanocopper ferrite and its green catalytic activity in alcohol oxidation reaction. *J. Supercond. Nov. Magn.* **2019**, *32*, 903–910.
48. Ali, I.O.; Mostafa, A.G. Photocatalytic reduction of chromate oxyanions on MMnFe₂O₄ (M= Zn, Cd) nanoparticles. *Mater. Sci. Semicond. Process.* **2015**, *33*, 189–198.
49. Elhenawy, A.A.; Al-Harbi, L.M.; El-Gazzar, M.A.; Khowdiary, M.M.; Moustfa, A. Synthesis, molecular properties and comparative docking and QSAR of new 2-(7-hydroxy-2-oxo-2H-chromen-4-yl) acetic acid derivatives as possible anticancer agents. *Spectrochim. Acta Part A Mol. Biomol. Spectrosc.* **2019**, *218*, 248–262. [[CrossRef](#)]
50. Fukui, K. Role of frontier orbitals in chemical reactions. *Science* **1982**, *218*, 747–754. [[CrossRef](#)]
51. Elhenawy, A.A.; Al-Harbi, L.M.; Moustafa, G.O.; El-Gazzar, M.A.; Abdel-Rahman, R.F.; Salim, A.E. Synthesis, comparative docking, and pharmacological activity of naproxen amino acid derivatives as possible anti-inflammatory and analgesic agents. *Drug Des. Dev. Ther.* **2019**, *13*, 1773–1790. [[CrossRef](#)]
52. Wildman, S.A.; Crippen, G.M. Prediction of physicochemical parameters by atomic contributions. *J. Chem. Inf. Comput. Sci.* **1999**, *39*, 868–873. [[CrossRef](#)]
53. Luque, F.J.; López, J.M.; Orozco, M. Perspective on “Electrostatic Interactions of a Solute with a Continuum. A Direct Utilization of ab Initio Molecular Potentials for the Prevision of Solvent Effects”. In *Theoretical Chemistry Accounts*; Springer: Cham, Switzerland, 2000; pp. 343–345.
54. Komorowski, L.; Lipinski, J.; Szarek, P.; Ordon, P. Polarization justified Fukui functions: The theory and applications for molecules. *J. Chem. Phys.* **2011**, *135*, 014109. [[CrossRef](#)]
55. Mendoza-Huizar, L.H.; Rios-Reyes, C.H. Chemical reactivity of atrazine employing the Fukui function. *J. Mex. Chem. Soc.* **2011**, *55*, 142–147.
56. Ali, I.O.; Salama, T.M.; Bakr, M.F.; El-Henawy, A.A.; Lateef, M.A.; Guma, H.A. Synthesis of nano-sized zeolite-Y functionalized with 5-amino-3-thiomethyl 1H-pyrazole-4-carbonitrile for effective Fe (III)-chelating strategy. *Res. Chem. Intermed.* **2018**, *44*, 5193–5222. [[CrossRef](#)]
57. Adant, C.; Dupuis, M.; Bredas, J. Ab initio study of the nonlinear optical properties of urea: Electron correlation and dispersion effects. *Int. J. Quantum Chem.* **1995**, *56*, 497–507. [[CrossRef](#)]
58. Handy, N.C.; Maslen, P.E.; Amos, R.D.; Andrews, J.S.; Murray, C.W.; Laming, G.J. The harmonic frequencies of benzene. *Chem. Phys. Lett.* **1992**, *197*, 506–515. [[CrossRef](#)]
59. Abraham, J.P.; Sajan, D.; Shettigar, V.; Dharmaparakash, S.M.; Němec, I.; Joe, I.H.; Jayakumar, V.S. Efficient π -electron conjugated push–pull nonlinear optical chromophore 1-(4-methoxyphenyl)-3-(3, 4-dimethoxyphenyl)-2-propen-1-one: A vibrational spectral study. *J. Mol. Struct.* **2009**, *917*, 27–36. [[CrossRef](#)]